Flow patterns in ascending aortic aneurysms

Determining the role of hypertension using phase contrast magnetic resonance and computational fluid dynamics

Ramaekers, M. J.F.G.; van der Vlugt, I. B.; Westenberg, J. J.M.; Perinajová, R.; Lamb, H. J.; Wildberger, J. E.; Kenjereš, S.; Schalla, S.

**DOI**

**Publication date**
2024

**Document Version**
Final published version

**Published in**
Computers in Biology and Medicine

**Important note**
To cite this publication, please use the final published version (if applicable).
Please check the document version above.

# Flow patterns in ascending aortic aneurysms: Determining the role of hypertension using phase contrast magnetic resonance and computational fluid dynamics

M.J.F.G. Ramaekers [a,b,1], I.B. van der Vlugt [c,1], J.J.M. Westenberg [d], R. Perinajová [c,e], H.J. Lamb [d], J.E. Wildberger [b,f], S. Kenjereš [c,e,*,2], S. Schalla [a,b,2]

[a] Departments of Cardiology and Radiology and Nuclear Medicine, Maastricht University Medical Center +, Maastricht, The Netherlands
[b] Cardiovascular Research Institute Maastricht (CARIM), Maastricht, The Netherlands
[c] Department of Chemical Engineering, Faculty of Applied Sciences, Delft University of Technology, Delft, The Netherlands
[d] Department of Radiology, Leiden University Medical Center, Leiden, The Netherlands
[e] J.M. Burgerscentrum Research School for Fluid Mechanics, Delft, The Netherlands
[f] Department of Radiology and Nuclear Medicine, Maastricht University Medical Center +, Maastricht, The Netherlands

## ARTICLE INFO

## ABSTRACT

Thoracic aortic aneurysm (TAA) is a local dilation of the thoracic aorta. Although universally used, aneurysm diameter alone is a poor predictor of major complications such as rupture. There is a need for better biomarkers for risk assessment that also reflect the aberrant flow patterns found in TAAs. Furthermore, hypertension is often present in TAA patients and may play a role in progression of aneurysm. The exact relation between TAAs and hypertension is poorly understood. This study aims to create a numerical model of hypertension in the aorta by using computational fluid dynamics. First, a normotensive state was simulated in which flow and resistance were kept unaltered. Second, a hypertensive state was modeled in which blood inflow was increased by 30%. Third, a hypertensive state was modeled in which the proximal and peripheral resistances and capacitance parameters from the three-element Windkessel boundary condition were adjusted to mimic an increase in resistance of the rest of the cardiovascular system. One patient with degenerative TAA and one healthy control were successfully simulated at hypertensive states and were extensively analyzed. Furthermore, three additional TAA patients and controls were simulated to validate our method. Hemodynamic variables such as wall shear stress, oscillatory shear index, endothelial cell activation potential (ECAP), vorticity and helicity were studied to gain more insight on the effects of hypertension on flow patterns in TAAs. By comparing a TAA patient and a control at normotensive state at peak-systole, helicity and vorticity were found to be lower in the TAA patient throughout the entire domain. No major changes in flow and flow derived quantities were observed for the TAA patient and control when resistance was increased. When flow rate was increased, regions with high ECAP values were found to reduce in TAA patients in the aneurysm region which could reduce the risk of thrombogenesis. Thus, it may be important to assess cardiac output in patients with TAA.

## 1. Introduction

Hypertension is a major risk factor for cardiovascular diseases. Dilatation of the aorta, also known as aortic aneurysm, is among these diseases. Not only is management of hypertension recommended in patients with aortic aneurysms, but hypertension is also among the criteria for preventative aortic surgery in patients with bicuspid aortic valves [1].

An aortic aneurysm is defined as local aortic dilatation of 150% with respect to the 'normal' aortic diameter [2]. Early diagnosis of an aortic aneurysm is critical, given the risk of severe and often fatal complications, such as aortic dissection or rupture. Since complication risk grows with increasing aortic size, routine imaging of thoracic aortic aneurysms (TAA) is necessary to follow up its diameter [3,4]. The complete etiology of TAA, however, is not fully understood. Nonetheless, a main risk factor for aortic disease is hypertension which should
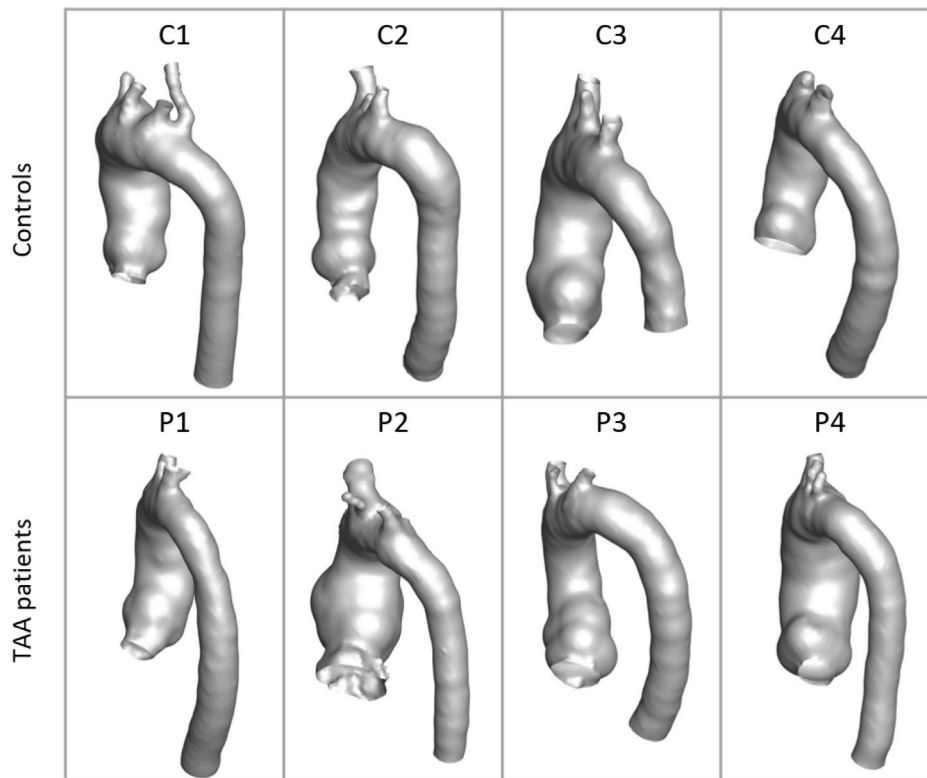
**Fig. 1.** Geometries obtained from MRI examination for four controls (C1, C2, C3, C4) and four TAA patients (P1, P2, P3, P4).

be monitored closely according to clinical guidelines. Moreover, the influence of other hemodynamic properties, such as velocity, wall shear stress (WSS), vorticity, and helicity, on the aneurysm pathology has been a major point of interest in literature [5–8]. Aberrant flow patterns and deviating WSS have been pointed out as potential contributors to vessel wall remodeling and aneurysm formation [5,9]. In degenerative ascending aneurysms, it is believed that there are major flow perturbations that lead to a deviant distribution of WSS [9]. However, to our knowledge, no studies have examined the influence of hypertension on flow-related parameters.

Blood flow can be analyzed in complex and patient-specific geometries through the use of computational fluid dynamics (CFD). Magnetic resonance imaging (MRI) is often used in combination with CFD since CFD yields higher spatial and temporal resolutions than MRI [10–12]. Such higher resolutions are preferable, especially at regions close to the arterial wall. Limited research was found that aimed at modeling hypertensive states and most studies did not present patient-specific models [13–15]. In the current study, the effects of hypertension on TAA hemodynamic were modeled by either increasing blood inflow or by altering the three-element Windkessel (3EWK) boundary condition. To our knowledge, the present work is the first study in which the Windkessel parameters have been varied to increase resistance in the aorta. The 3EWK boundary condition has gained support in recent years and is based on a patient-specific adaptation of a three-element electric circuit analog [16–18]. The Windkessel model is a widely used outlet boundary condition and describes the heart and arteries as a closed hydraulic system. A 3EWK model consists of three model coefficients (so-called RCR-parameters): proximal resistance ($R1$), peripheral or distal resistance ($R2$) and compliance ($C$). The proximal resistance is caused by fluid friction in the domain of interest. The peripheral resistance is mainly ascribed to the smaller arteries downstream. The compliance represents the capacity of the aorta to expand and contract. By using a 3EWK model it was possible to incorporate changes to resistance and aortic compliance in our CFD simulations to mimic hypertensive states.

In the current study, we described the effects of hypertension on the following flow-related parameters: velocity, WSS, time-averaged WSS (TAWSS), oscillatory shear index (OSI), endothelial cell activation potential (ECAP), Q-criterion, vorticity and helicity in TAA patients and controls. We have extensively analyzed one TAA patient and one healthy control, and have included three additional TAA patients and controls to show the numerical robustness and adaptability of the developed approach.

## 2. Methods

### 2.1. Study population

Four patients with degenerative TAA with a diameter of 40 mm or larger who underwent MRI examination for aneurysm follow up were retrospectively included at random. From the included subjects, one from each group was chosen randomly to perform the extensive analysis. The other subjects were used to validate the method. All participants provided informed consent. Exclusion criteria consisted of prior aortic or cardiac surgery, presence of connective tissue disease or general contra-indications for MRI. Patients with atrial fibrillation were excluded to ensure MRI accuracy. Four age-matched-subjects without any cardiac or aortic disease were included as a control group.

### 2.2. MRI acquisition

All patients and controls underwent MRI examinations on 3-T MR systems (Philips Ingenia; Philips Healthcare, Best, the Netherlands). The imaging protocol included four-dimensional (4D) phase contrast imaging covering the volume of the thoracic aorta. All parameters of the 4D flow sequence are listed in Table 1. Data were acquired using retrospective ECG gating and navigator respiratory gating based on diaphragm excursion. Directly after MRI examination, blood pressure (BP) was acquired from both arms whilst the subject was still in supine position.

**Table 1**

4D flow MRI parameters. FOV, field of view; TE, echo time; TR, repetition time; VENC, velocity encoding.

| | |
|---|---|
| FOV [mm] | $450 \times 298 \times 68$ |
| Acquired voxel size [mm] | $2.5 \times 2.5 \times 2.5$ |
| Reconstructed voxel size [mm] | $1.41 \times 1.41 \times 2.5$ |
| Flip angle [degrees] | 10 |
| TE [ms] | 2.7 |
| TR [ms] | 4.6 |
| K-space segmentation factor [–] | 2 |
| SENSE factor [–] | 2.5 (P) x 1.2 (S) |
| VENC [cm/s] | 150–175* |
| (Reconstructed) cardiac phases [–] | 24–34 |
| Temporal resolution [ms] | 36.8 |

\* Or higher in case of aortic valve stenosis in patient.

## 2.3. Geometry and numerical mesh

4D flow MR images were analyzed using commercially available software (CAAS MR Solutions 5.2.1; Pie Medical Imaging, Maastricht, the Netherlands). Geometries including the supra-aortic arteries were segmented in peak-systole semi-automatically from 4D flow MR images and manually adjusted if deemed necessary, Fig. 1. Peak-systole was defined as the phase with the highest flow rate on 4D flow MR. The patient specific geometries were exported as a STL file. The Vascular Modeling Toolkit (VMTK) was used to process the obtained geometries for computational purposes [19]. The geometries were cut and Taubin smoothed as shown in Figs. 2(A–B). The cuts were orthogonal to the direction of the flow field and were executed at the inlet and all outlets. A smoothing factor of 0.01 with 100 iterations was used. To stabilize the flow, flow extensions of 6 times the radius were added to all outlets, whereas the inlet was left unaltered. Subsequently, the geometries were meshed in Ansys ICEM CFD 2021 R2 (Ansys, Canonsburg, Pennsylvania). First, an unstructured mesh of tetrahedral elements was created with a layer of 10 prism elements at the wall. At the inlet the ratio of the thickness of the first control volume at the wall and the inlet diameter was $2.4 \times 10^{-3}$. At the outlet this ratio was $3 \times 10^{-3}$. The obtained meshes were converted to polyhedral meshes in Ansys Fluent 2021 R2 (Ansys, Canonsburg, Pennsylvania). Fig. 2(C) shows an example of a meshed geometry. Grid sizes varied between 730,000 and 1,100,000 elements. An extensive mesh sensitivity analysis was performed to assess the accuracy of the simulations (see Appendix A).

## 2.4. Solver settings

The numerical models were based on the continuity equation and the 3D unsteady Navier–Stokes equations for incompressible flow, which can be written as:

$$\frac{\partial u_i}{\partial x_i} = 0 \tag{1}$$

$$\rho \frac{\partial u_i}{\partial t} + \rho u_j \frac{\partial u_i}{\partial x_j} = -\frac{\partial p}{\partial x_i} + \frac{\partial}{\partial x_j}\left(\mu \frac{\partial u_i}{\partial x_j}\right) + F_i \tag{2}$$

where $u_i$ is the velocity, $p$ is the pressure, $F_i$ is the external force, $\rho$ is the density, and $\mu$ is the dynamic viscosity. Blood was assumed to be a single-phase fluid with a constant density ($\rho = 1060$ kg/m$^3$) and non-Newtonian viscosity. The blood rheology (i.e the shear-rate dependent dynamic viscosity) was modeled by using the Carreau-Yasuda model because of its simplicity and carefully calibrated model coefficients:

$$\frac{\mu - \mu_\infty}{\mu_0 - \mu_\infty} = \left[1 + (\lambda \dot{\gamma})^a\right]^{\frac{n-1}{a}} \tag{3}$$

where the model coefficients are given in Table 2.

The governing equations were discretized using the finite-volume based second order discretization in space (i.e. central-difference scheme (CDS) for diffusive term and the second-order upwind for the
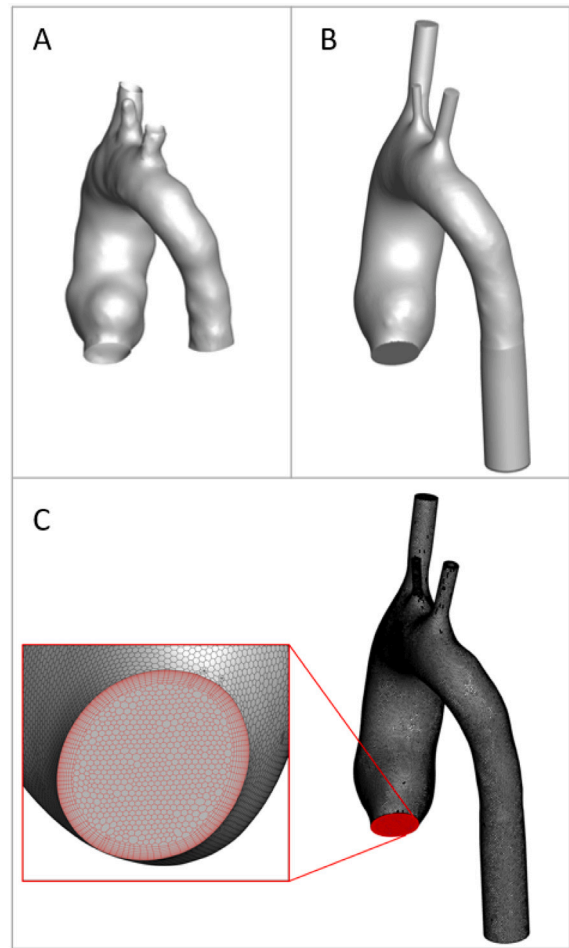


**Fig. 2.** Example of geometry before (A) and after (B) processing in Vascular Modeling Toolkit (VMTK) and polyhedral mesh with front view of the inlet (C).

**Table 2**

Coefficients of the Carreau-Yasuda model adopted from [20].

| $\mu_\infty$ mPa s | $\mu_0$ mPa s | $\lambda$ s | $a$ – | $n$ – |
|---|---|---|---|---|
| 3.14 | 213.1 | 50.2 | 0.8588 | 0.331 |

convective terms). The transient formulation was second order implicit with a time step of $\Delta t = 1$ ms. Pressure–velocity coupling was performed by the SIMPLE algorithm. An under-relaxation factor of 0.1 and 0.5 was used for pressure and momentum, respectively. Furthermore, laminar flow was assumed for all simulations. The simulations were started at peak-systole. First, four cardiac cycles were run where the residual for solution was kept at $10^{-3}$ in order to stabilize flow and pressure. Subsequently, a fifth cycle with a residual of $10^{-4}$ was performed to obtain fully converged temporal results. The numerical integration was carried out using Ansys Fluent 2021 R2 (Ansys, Canonsburg, Pennsylvania). Simulations were run on 64–128 cores. The time to complete simulations varied between 2–5 days, depending on the model and the geometry. The overview of solution method are presented in Table 3.

## 2.5. Boundary conditions

The model consists of one inlet and, depending on the subject, 3 to 5 outlets as depicted in Fig. 3.
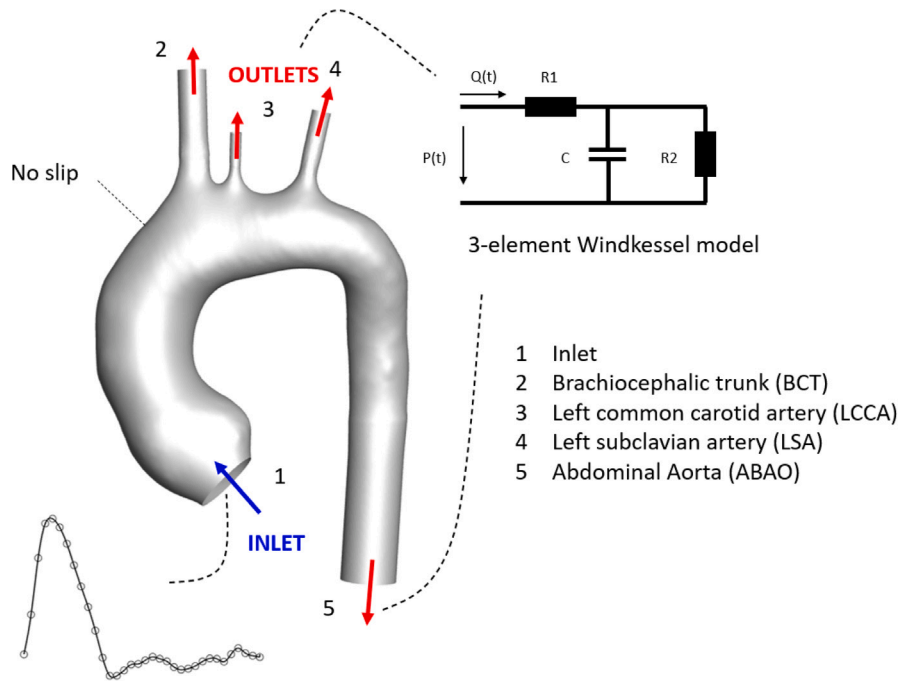
**Fig. 3.** Selected boundary conditions for inlet, outlets and wall. At the inlet a patient-specific mass flow rate is prescribed. The 3-element Windkessel model is used as outlet boundary condition.

**Table 3**
Solution method details selected in Ansys Fluent.

| Pressure–velocity coupling | |
| --- | --- |
| Scheme | SIMPLE |
| Flux Type | Rhie-Chow: distance-based |
| Spatial discretization | |
| Gradient | Least squares cell-based |
| Pressure | Second order |
| Momentum | Second order upwind |
| Transient formulation | Second order implicit |

**Table 4**
Three-element Windkessel model parameters for each outlet for a healthy person (C3). The values of proximal resistance ($R1$), peripheral resistance ($R2$) and capacitance ($C$) are tuned based on the procedure described by [21].

| Parameter | $R1 \cdot 10^{-8}$ Pa s/m$^3$ | $R2 \cdot 10^{-8}$ Pa s/m$^3$ | $C \cdot 10^{10}$ m$^3$/Pa |
| --- | --- | --- | --- |
| Brachiocephalic trunk | 0.985 | 9.96 | 24.4 |
| Left common carotid artery | 4.82 | 48.7 | 4.99 |
| Left subclavian artery | 3.33 | 33.7 | 7.21 |
| Abdominal aorta | 0.323 | 3.27 | 74.3 |

### 2.5.1. Inlet — patient-specific velocity profile

At the inlet of the aorta, a patient-specific mass flow rate is prescribed. The mean temporal velocities obtained from MRI examination were used to specify a plug flow profile. In order to apply the inlet profile to the solver, a user-defined function (UDF) was created. Spline interpolation was performed to fit against the raw MRI data.

### 2.5.2. Outlets — three-element Windkessel model

The Windkessel model is a widely used outlet boundary condition and describes the heart and arteries as a closed hydraulic system. When applied to the cardiovascular system the Windkessel can be interpreted as an elastic reservoir. When used in a numerical simulations, the Windkessel model correlates the outlet pressure to the corresponding flow rate. Hence, the calculated pressure is imposed as a boundary condition to the outlet. Mathematically, the 3EWK model is described by the following expressions:

$$P^n = \frac{(R1 + R2 + R1 \cdot \beta)Q^n + \beta \cdot P^{n-1} - R1 \cdot \beta \cdot Q^{n-1}}{1 + \beta},$$
$$\beta = \frac{R2 \cdot C}{\Delta t} \tag{4}$$

where $P(t)$ is the pressure, $Q(t)$ the flow rate, ($n$) and ($n-1$) indicate values from the current and previous time steps, respectively. The RCR-parameters were estimated based on method 2 described by [21]. For the different controls and patients, a set of systolic-diastolic blood pressures was available together with 4D flow data at the outlets from

MRI examination. The obtained RCR-parameters for a control (C3) are presented in Table 4. An UDF was created to implement the 3EWK boundary condition in the model. In Ansys Fluent the relative (or gauge) pressure is calculated. The calculated pressure was found to not directly match with the measured systolic and diastolic blood pressures (SBPs and DBPs). Therefore, the pressure was scaled to generate systemic pressures that corresponded to the measured blood pressure. The pressure wave forms were scaled with respect to the SBP. A scaling factor ($SF$) was specified that equaled the difference between the calculated pressure ($P_{solver}$) and the measured pressure ($P_{measured}$) at peak-systole ($PS$) as:

$$SF = P_{solver}^{PS} - P_{measured}^{PS} \tag{5}$$

The systemic pressure ($P$) is then defined as:

$$P = P_{solver} - SF \tag{6}$$

Hence, the SBP calculated in the current model equals the measured SBP.

### 2.5.3. Wall

The no-slip boundary condition was selected for the wall. Unlike a real aorta, the wall was also assumed to be rigid. However, we hypothesize that the 3EWK boundary condition used in the current model can to a certain extend compensate for the absence of wall elasticity.

## 2.6. Hemodynamic parameters

For the current study, eight quantitative variables were used to understand the effects of hypertension: velocity ($\vec{u}$), WSS, TAWSS, OSI, ECAP, vorticity ($\vec{\omega}$), helicity ($H$) and Q-criterion. The wall shear stress is calculated as:

$$\vec{\tau}_w = \mu \cdot \dot{\gamma}_w = \mu \frac{\partial \vec{u}}{\partial n}|_{\text{wall}} \qquad (7)$$

Furthermore, TAWSS was obtained by time-averaging WSS over one cardiac cycle as:

$$\text{TAWSS} = \frac{1}{T} \int_0^T |\vec{\tau}_w| dt \qquad (8)$$

OSI is an index which describes the degree of deviation of the WSS from its average direction. Hence, OSI is a measure of WSS oscillation during a cardiac cycle and is defined as:

$$\text{OSI} = \frac{1}{2} \left( 1 - \frac{|\int_0^T \vec{\tau}_w dt|}{\int_0^T |\vec{\tau}_w| dt} \right) \qquad (9)$$

The metric ECAP takes the effects of both low WSS and high OSI into account and is expressed as:

$$\text{ECAP} = \frac{\text{OSI}}{\text{TAWSS}} \qquad (10)$$

The vorticity vector was defined as:

$$\vec{\omega} = \nabla \times \vec{u} \qquad (11)$$

Helicity in blood flow was defined as:

$$H = \vec{u} \cdot (\nabla \times \vec{u}) = \vec{u} \cdot \vec{\omega} \qquad (12)$$

Mean values of velocity magnitude, WSS, vorticity and helicity were calculated. Additionally, the Q-criterion (i.e. the second invariant of the velocity gradient tensor) which quantifies vortex-core structures was computed. Positive values of the Q-criterion are indicative of regions where the local flow rotation dominates over its shear.

## 2.7. Parameter selection

For each case three states were simulated. First, a base case (BC) in which flow and pressure were kept unaltered. Second, a hypertensive state in which blood inflow was increased with 30% (HYP-Q). Third, a hypertensive state in which the RCR-parameters from the 3EWK boundary condition were adjusted to mimic an increase in resistance (HYP-RCR). The two hypertension models (HYP-Q and HYP-RCR) were first developed for one control (C3). The measured BP values of the individual were 118/81 mmHg. After running the base case simulation in which inflow and resistance were unaltered (BC), the calculated pressure at peak-systole was scaled to the measured value at peak-systole. This resulted in pressure values of 118/68.5 mmHg. It was aimed to obtain values around 160/90 mmHg for virtual hypertension. An increase in peripheral resistance ($R2$) was expected to be the predominant cause of elevated BP. Additionally, in the parameter study we found that increasing the proximal resistance ($R1$) resulted in an increase of the pulse pressure which is also observed in hypertension. Furthermore, increasing resistance is associated with decreasing elasticity of the arteries. Therefore, capacitance ($C$) was reduced in HYP-RCR. We found that using $1.5 \times R1$, $1.75 \times R2$ and $0.9 \times C$ resulted in 168/95 mmHg for C3. These changes in RCR-parameters were used for HYP-RCR (see Table 5). In this paper the results from the three models (BC, HYP-Q and HYP-RCR) are shown for one control (C3) and one TAA patient (P5). They will simply be referred to as control and TAA patient from now on. The detailed study of the 3EWK model for the HYP-RCR method and its sensitivity on the RCR parameters is presented in Appendix B.

**Table 5**

Parameter selection for the base case (BC) and two hypertension models (HYP-Q and HYP-RCR).

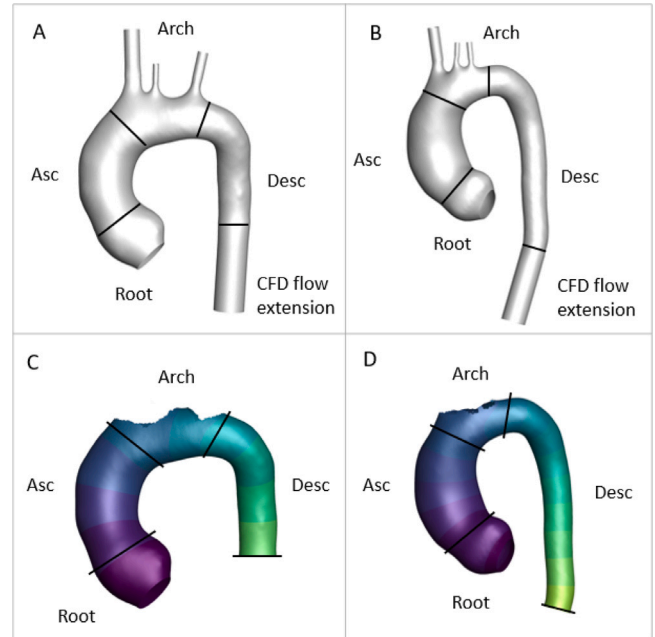|  | $R1$ | $R2$ | $C$ | Inflow |
|---|---|---|---|---|
| BC | ×1 | ×1 | ×1 | ×1 |
| HYP-Q | ×1 | ×1 | ×1 | ×1.3 |
| HYP-RCR | ×1.5 | ×1.75 | ×0.9 | ×1 |



**Fig. 4.** Segmentation of the geometry for the (a) control and (b) TAA patient in: root, ascending aorta (Asc), aortic arch and descending aorta (Desc). The top outlets were removed from the aortic arch ((c) and (d)). Note that the drawn black lines used for indicating the segments are illustrative and were actually more curved (not straight).

## 2.8. Data analysis

In total eight cases were run (four controls and four TAA patients) which resulted in 24 simulations. Quantified data from all hemodynamic parameters of interest were exported in four different segments (root, ascending aorta, aortic arch, and descending aorta) and three different phases of the cardiac cycle (peak-systole, end-systole, and mid-diastole). Peak-systole was defined as the cardiac phase with highest flow rate, end-systole was defined as halfway between peak-systole and the beginning of diastole. The beginning of diastole was specified as the point in time when the forward flow returned to zero. The domain was subdivided using longitudinal metric calculated by VMTK (abscissa metric and stretched mapping). The partitioning of the surface into arterial branches occurred through the delineation of intersections between the primary center-line and the specific center-line corresponding to the given branch. The resulting geometries for the control and TAA patient are shown in Fig. 4. Velocity, WSS, vorticity and helicity were analyzed for the different anatomical segments.

## 2.9. Workflow

The workflow is illustrated in Fig. 5. From MRI examination, patient-specific geometries and 4D flow data were retrieved together with the SBPs and DBPs. Once the geometries were prepared, meshes were created and boundary conditions were applied. For the 3EWK outlet boundary condition, the mean pressure and mean flow rate from the examination were required to calculate the RCR-parameters. After the simulations, a mesh independence study was carried out and the
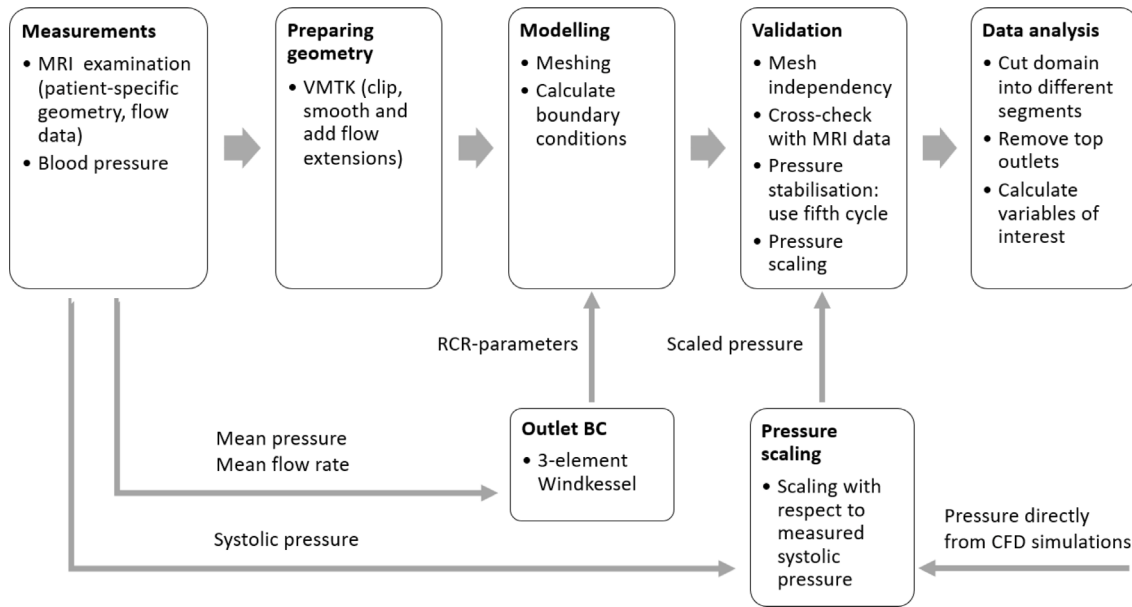
**Fig. 5.** Workflow adopted for present study. CFD: computational fluid dynamics, MRI: Magnetic resonance imaging, VMTK: Vascular Modeling Toolkit.

results were cross-checked with MRI data. The pressure from the CFD simulations was scaled with respect to the measured systolic pressure. Lastly, the domain was segmented and the top outlets were removed in order to calculate all variables of interest.

## 3. Results

### 3.1. Pressure

Pressure was monitored in the descending aorta at one point on the centerline — line above the flow extension, as shown in Figs. 6, 7. Both the control and TAA patient had similar BP values of 118/81 and 125/85 mmHg, respectively. They responded similarly to the hypertension models HYP-Q and HYP-RCR. The obtained pressure wave forms for HYP-Q show that an increase of 30% in inflow did not result in an increase of BP, Figs. 6 and 7. However, the pressure distributions at peak-systole show that the pressure is slightly higher in the root, ascending aorta and aortic arch for HYP-Q. In the descending aorta, where pressure is monitored, pressure is unaltered. For HYP-RCR, BP values of 168/95 and 160/111 were obtained for the control and TAA patient, respectively, resulting in virtual hypertension. From Figs. 6 and 7, it can be seen that the pressure distributions at peak-systole between BC and HYP-RCR are similar.

### 3.2. Q-criterion

To improve visualization of the unsteady flow features, Fig. 8 shows snapshots of the flow pattern in terms of vortex strength at peak-systole, end-systole and mid-diastole, respectively. The vortex strength is visualized by using the Q-criterion. The results are depicted for an iso-surface of $Q = 1000$ $1/s^2$ and colored by the rotational direction around the vertical axis ($\omega_z$). It was found that the peak-systolic vortex strength in the control was higher compared to the TAA patient. Especially in the ascending aorta lower peak-systolic vortex strength was observed in the TAA patient. For both the TAA patient and the control the vortices were strongest in the inner curvature of the aorta. Furthermore, the control and TAA patient reacted similarly to the two hypertensive states. When flow rate increased (HYP-Q), the peak-systolic vortex strength increased, but no major changes in flow occurred. Additionally, it was found that increasing resistance (HYP-RCR) produced results similar to BC. The individual vortex structures

were better visible at end-systole where the effects of the wall are more filtered out. The flow was characterized by highly rotational flow fields. Again, the control appeared to have higher vortex strength, especially in the ascending aorta. Moreover, the vortices were again primarily observed at the inner curvature. At end-systole also a strong helical motion downstream (in the descending aorta) was observed. At mid-diastole, due to the absence of strong streamwise flow, residual vorticity effects dominate. Quite different bulk flow was observed at mid-diastole with lower vorticity values in the XY-plane. Furthermore, considerably more vortex structures were present in the ascending aorta of the TAA patient compared to the control at mid-diastole. The extent to which flow traveled along the aorta was also reduced during diastole.

### 3.3. TAWSS, OSI and ECAP

The metrics TAWSS, OSI and ECAP were computed for the control, Fig. 9, and the TAA patient, Fig. 10. The higher velocities from HYP-Q were found to lead to larger TAWSS magnitudes. TAWSS magnitudes for HYP-RCR and BC appeared to be similar. However, the lower velocities from BC and HYP-RCR led to more regions that are influenced by higher OSI in the TAA patient, especially in the aneurysmatic region. Less significant changes in OSI were observed in the control. Given the values of TAWSS and OSI, maximum ECAP was found to be higher in the TAA patient with the largest values of ECAP found at the outer curvature in the aneurysmatic region. In the control ECAP was below 0.6 $Pa^{-1}$ throughout the entire domain. It was found that ECAP almost reached 1.4 $Pa^{-1}$ in small regions for the TAA patient when flow rate was not increased (BC and HYP-Q). Additionally, the locations with high ECAP values differed between BC and HYP-Q, as shown in Fig. 11.

### 3.4. Segmentation per sections

#### 3.4.1. Velocity

The mean velocity magnitudes in the different segments for the control and TAA patient at peak-systole are shown in Fig. 12. In the patient lower mean velocity magnitudes were observed. Mean velocities were found to decrease towards the ascending aorta and then increase towards the descending aorta in both the control and the TAA patient. Additionally, the control and TAA patient responded similar to an increase in inflow rate (HYP-Q) with increased mean velocities. Furthermore, no changes were observed when resistance had been increased (HYP-RCR) for the control and TAA patient.
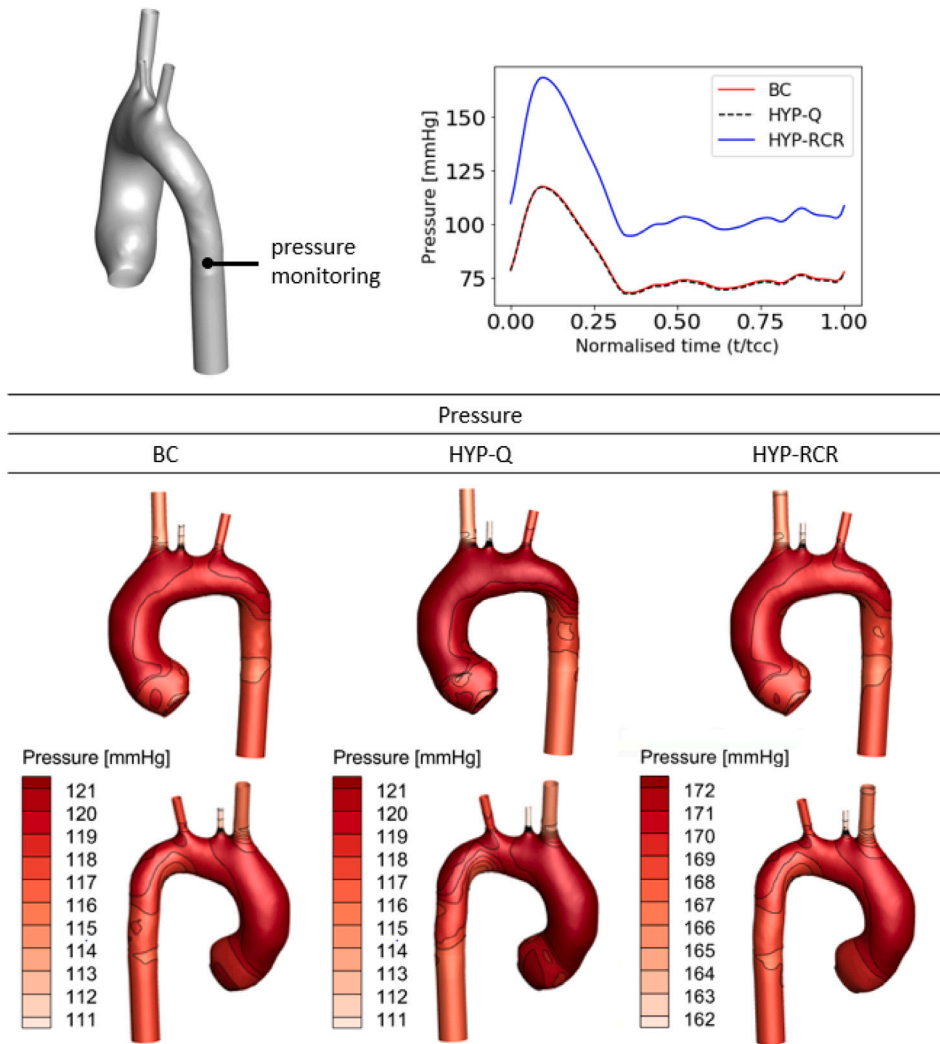
**Fig. 6.** Pressure waveforms and pressure distributions for the base case (BC) and two hypertension models (HYP-Q and HYP-RCR) at peak-systole in control. Note the different scaling for HYP-RCR.

### 3.4.2. WSS

Lower mean WSS values were observed in the TAA patient. The tend of mean WSS at peak-systole over the different segments was similar to velocity Fig. 12. The lowest mean values of WSS were found in the ascending aorta. Again, mean WSS increased for the control and TAA patient when flow rate had been increased (HYP-Q). Additionally, minimal changes in WSS were observed for the control and TAA patient when resistance was increased (HYP-RCR).

### 3.4.3. Vorticity

Vorticity plays an important role in maintaining stable flow through the aorta since low vorticity values can result in aberrant flow patterns. Similar to the velocity magnitude at peak-systole, the mean vorticity was also observed to be the lowest in the ascending aorta, Fig. 12. Compared to the mean velocity magnitude, the three models (BC, HYP-Q, HYP-RCR) now converged towards the descending aorta. Again higher flow rates (HYP-Q) resulted in higher mean vorticity values for the control and TAA patient. BC and an increase in resistance (HYP-RCR) still produced similar mean vorticities.

### 3.4.4. Helicity

Alike vorticity, helical flow patterns are crucial for maintaining stable aortic flow patterns. Helicity is derived from both the velocity and the vorticity vector and changes rotation direction when its sign changes. The control and TAA patient showed different trends in mean helicity over the different segments at peak-systole, Fig. 12. Overall, mean helicity was found to be lower in the TAA patient. Furthermore, when flow rate increased (HYP-Q), the range of the mean helicity increased for both the control and TAA patient.

## 4. Discussion

In this study, we have developed a method to model virtual hypertension by either increasing inflow with 30% (HYP-Q) or by adjusting the proximal and peripheral resistances and capacitance parameters from the 3EWK boundary condition to mimic an increase in resistance of the rest of the cardiovascular system (HYP-RCR). One TAA patient and one healthy control were successfully simulated at hypertensive states and were extensively analyzed. Limited research was found in which hypertension was modeled by using CFD. Sarrami-Foroshani et al. have successfully modeled hypertension in intracranial aneurysms by increasing both the inflow and the pressure at the outlets [13]. Their model was however not patient-specific and obtained from a 1D circulation model that was validated against a young individual. Furthermore, Vasava and co-workers have modeled hypertension in the aortic arch in an idealized geometry [14]. They deployed a pulsatile pressure as inlet and outlet boundary conditions and increased the cross-sectional area of the ascending aorta with increasing pressure. Moreover, Singh et al. have used CFD to study the effects of hypertension on aneurysmatic hemodynamics by altering blood viscosity values [15]. In our work,
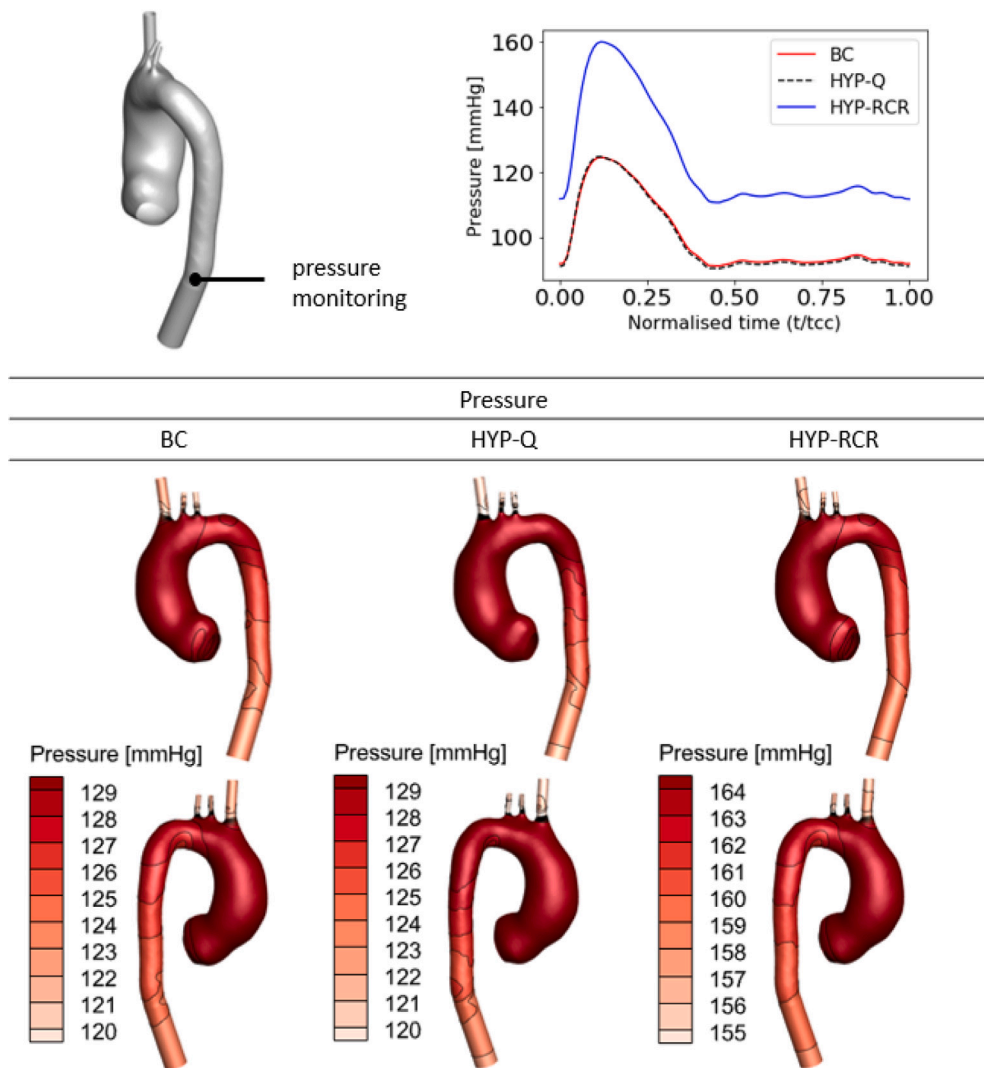
**Fig. 7.** Pressure waveforms and pressure distributions for the base case (BC) and two hypertension models (HYP-Q and HYP-RCR) at peak-systole in TAA patient. Note the different scaling for HYP-RCR.
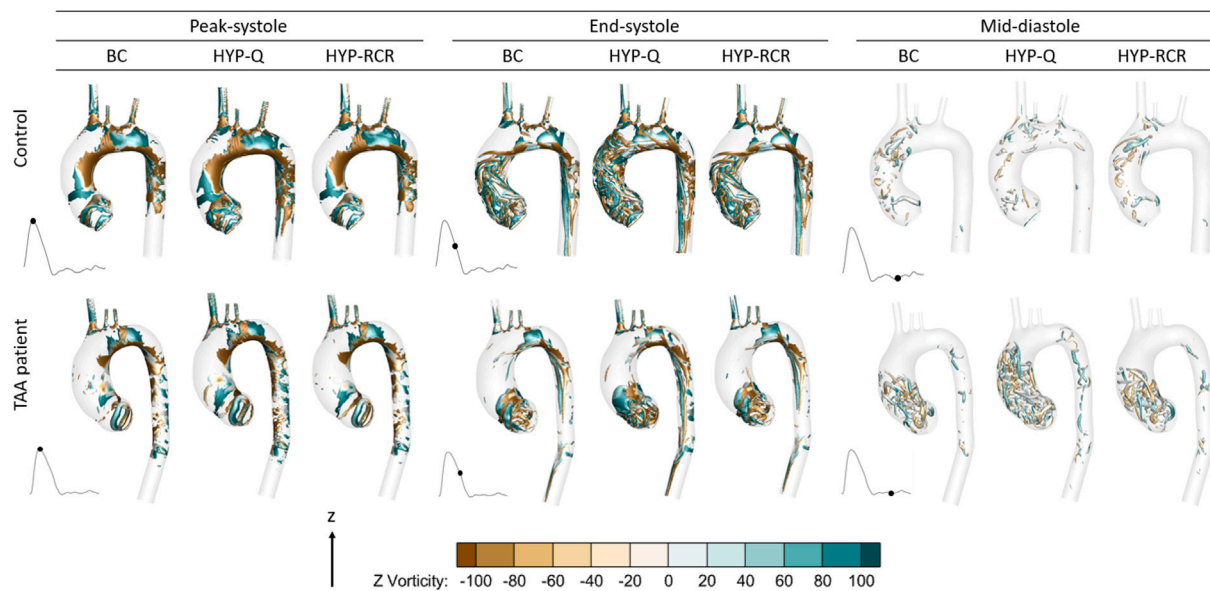


**Fig. 8.** Iso-surface of Q-criterion (1000 1/s$^2$) for control and TAA patient at peak-systole, end-systole and mid-diastole.
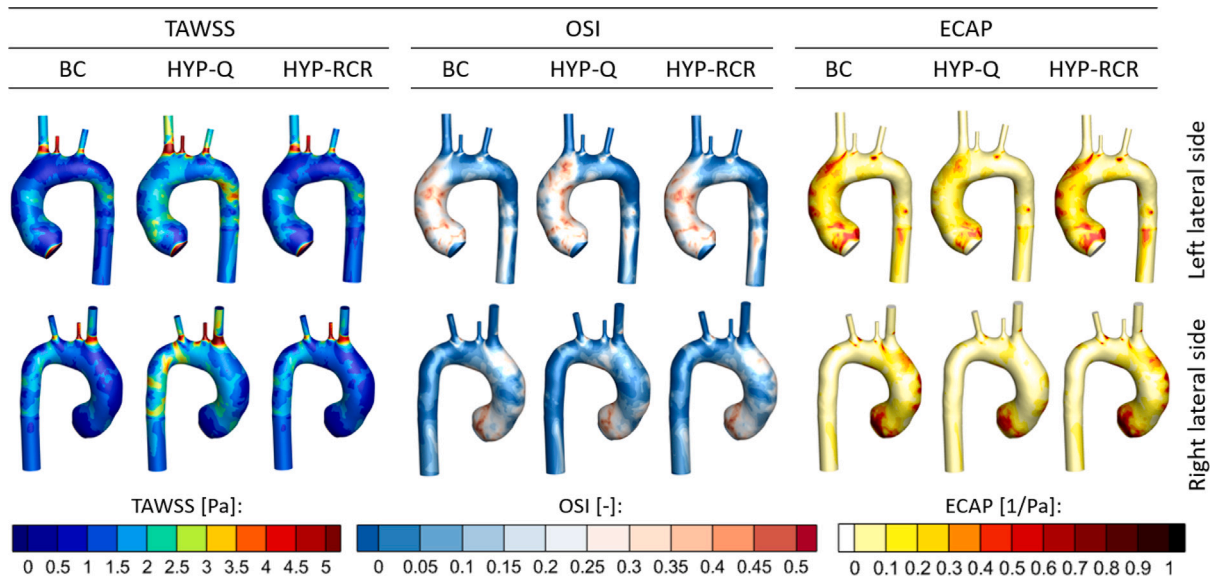
**Fig. 9.** Time averaged wall shear stress (TAWSS), oscillatory shear index (OSI) and endothelial cells activation potential (ECAP) for the base case (BC) and two hypertension models (HYP-Q and HYP-RCR) in control.
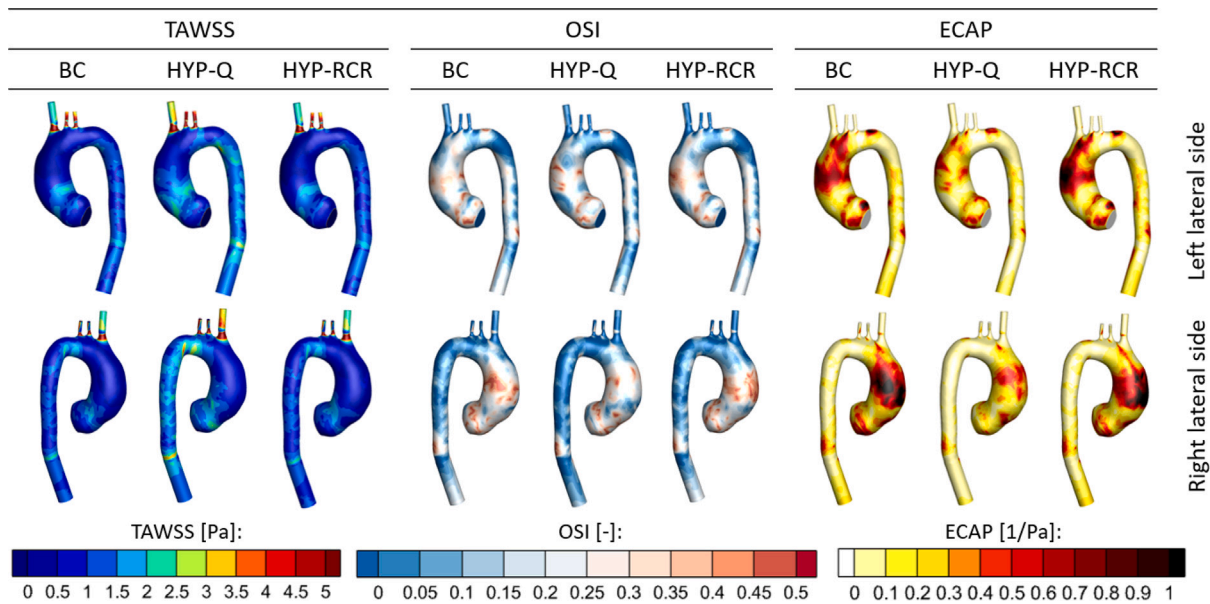


**Fig. 10.** Time averaged wall shear stress (TAWSS), oscillatory shear index (OSI) and endothelial cells activation potential (ECAP) for the base case (BC) and two hypertension models (HYP-Q and HYP-RCR) in TAA patient.

patient-specific geometries were used and it was possible to also apply patient-specific boundary conditions by exploiting the 3EWK model. Hence, we believe that the model developed in this work could be used to simulate more realistic hypertensive states in patients compared to previous work.

### 4.1. Influence of hypertension on aortic flow

In the current study, virtual hypertension was modeled by either increasing inflow (HYP-Q) or increasing resistance (HYP-RCR). It was found that increasing resistance resulted in only minor changes to flow and flow derived quantities in both the TAA patient and control. Additionally, increasing only flow rate did not result in a pressure increase which was expected since pressure was kept constant by

calculating the 3EWK model parameters. The pressures obtained from HYP-Q are therefore less realistic. However, the other hemodynamics obtained from this model are still useful. In reality, a combination of increased flow rate and resistance is believed to be present in hypertension [22]. Moreover, patients with increased resistance (due to aortic stiffness or ageing), also have reduced elasticity which influences flow [23,24]. This effect is not included in our study. By using a dynamic (non-rigid) wall boundary condition the flow differences in TAA patients could be more pronounced in the cases with elevated resistance. We believe that the impact of increasing resistance together with decreasing elasticity of the aortic wall is underestimated in our work. We therefore hypothesize that the minimal differences that are now observed in hemodynamic variables, especially in helicity, could be considerably larger in reality. A model in which flow and resistance
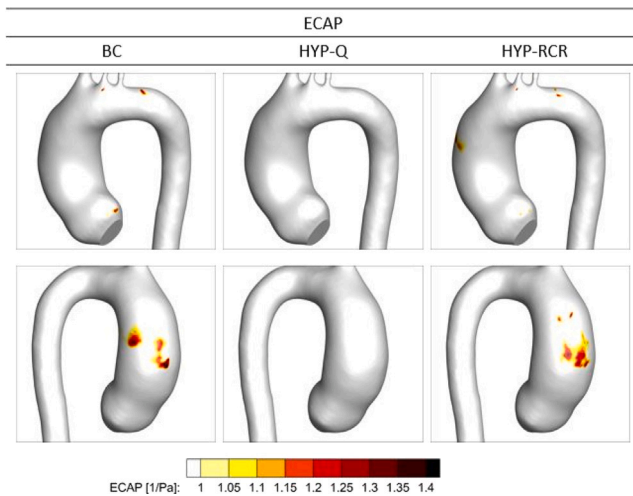
**Fig. 11.** Highest values (1–1.4 Pa$^{-1}$) of endothelial cells activation potential (ECAP) for the base case (BC) and two hypertension models (HYP-Q and HYP-RCR) in TAA patient.

are both increased to simulate a hypertensive state, is suspected to show more discrepancies in the hemodynamics of TAAs.

The ratio between OSI and TAWSS, ECAP, highlights the regions that are susceptible to thrombogenesis. It has been postulated that for TAWSS values below 0.36 Pa, monocytes are prone to adhere to endothelial cells which could lead to thrombogenesis [25,26]. Furthermore, OSI is a measure of how much the WSS vector changes in direction from its average direction during a cardiac cycle. High values of OSI indicate regions with disturbed flow at the vascular wall. Hence, an ECAP value around 1.4 Pa$^{-1}$ was considered by Deyranlou to be a threshold value for thrombogenesis [21]. Interestingly, when flow rate increased, ECAP lowered in the TAA patient and no regions with a value around 1.4 Pa$^{-1}$ were visible, Fig. 11. If hypertension occurs due to an increase in flow rate, this would not necessarily be an adverse effect in the context of thrombogenesis risk for the analyzed TAA patient.

### 4.2. Differences between control and TAA patient

Aberrant flow patterns are of great interest in aortic diseases. In this study, Fig. 8 clearly showed the presence of vortices in the TAA patient and control. High vorticity strength was mainly located in the inner curvature in the control at peak-systole which was also found in a study from Ramaekers et al. [9]. Higher vortex strength in the inner curvature was also observed in the TAA patient, which was not observed by Ramaekers et al. Vorticity and helicity were found to be lower for a TAA patient compared to a control which is in agreement with Ramaekers et al. but not with Burk et al. [5]. Only at mid-diastole, more vortex structures were observed for a TAA patient in this work.

Ramaekers et al. [9] postulated that with decreasing vorticity and helicity the risk of flow abnormalities like flow separation increases. They suggested that flow separation could cause lower and slower vortices in TAA patients. These type of vortices could lead to unequal WSS distributions with a higher risk of atherosclerosis on wall segments that experience low WSS. In our work, we observed significantly lower vortex strengths in the ascending aorta for the TAA patient at peak-systole.

Both high and low values of WSS have been associated with wall weakening and rupture [27,28]. In vitro studies showed that high WSS values contribute to aortic dilation and low WSS values to atherosclerosis [29–32]. High WSS values were found to cause adapted gene expression in endothelial cells after which endothelial cells proliferate

and the extracellular matrix degrades which leads to aneurysm formation [29]. Nonetheless, studies have also suggested that aneurysm rupture occurs at regions with low WSS [33].

Comparing our results to Burk et al. [5], it was also observed that WSS was significantly lower in all aortic segments during peak-systole in a TAA patient Fig. 12. However, due to aberrant flow patterns, not only peak-systole should be analyzed since such patterns occur more towards end-systole [34]. In our work, WSS and TAWSS were found to be lower in the TAA patient. Higher OSI values were observed in the ascending aorta in the TAA patient Fig. 10. ECAP values close to 1.4 Pa$^{-1}$ were found in the TAA patient mainly in the outer curvature of the ascending aorta Fig. 10. The regions with elevated ECAP values were small in the TAA patient, but ECAP values in the control were significantly lower, Fig. 9. This could indicate that the TAA patient has an elevated risk for thrombogenesis.

### 4.3. Clinical impact

Our model allows for predicting the effects of hypertension on aortic aneurysms. An interesting finding in our research is the normalization of OSI and ECAP in TAA patients in the HYP-Q model. A hypothesis could be that due to the increased volume in an aortic aneurysm, a larger stroke volume is needed to create sufficient secondary flow patterns to maintain stable flow. Callaghan et al. [35] found for example that helicity is one of the major factors to maintain stable aortic flow and that helicity is affected by stroke volume. Considering many aneurysm patients receive anti-hypertensive medication, which in some cases also reduces stroke volume, this finding would be of great interest to investigate in patients with and without anti-hypertensive medication.

### 4.4. Limitations of the present study

Some limitations of the present work should be addressed. First, the aortic wall was modeled as a rigid wall. Previous studies have shown that the rigid wall assumption is acceptable in normotensive blood flow simulations since general flow characteristics and WSS are not significantly affected by arterial compliance [36–39]. Furthermore, long-term hypertension can induce thickening of arterial walls and causing stiffness [40]. Therefore, we speculate that modeling the aortic wall as a rigid wall is more suited at hypertensive states compared to healthy aortas at normotensive states. Consequently, since our analysis did not include functional wall properties, possible variations in vessel wall thickness were not included in this study. Moreover, the used geometries were derived from peak-systole. Our approach in which the aortic wall is assumed to be rigid hence neglects potential movements of the aorta during a cardiac cycle and distensibility of the ascending aorta. However, data analysis was performed at peak-systole (except for TAWSS, OSI and ECAP).

Second, previous studies have shown that the diameter of the aorta changes when blood pressure changes [41,42]. Hypertension has been modeled with a dilation of the aorta by Vasava et al. [14]. In this work, no change in aortic diameter was taken into account, since it is believed that an aneurysm could already be a consequence of pressure increase. However, for the controls, an increase in aortic diameter would be expected.

Furthermore, a plug flow profile was prescribed at the inlet which is a commonly used spatial distribution [16]. However, the selection of the inlet boundary condition significantly affects the flow (close to the inlet) [43–45]. It could therefore be more accurate to prescribe a more patient-specific boundary condition to the inlet such as a 3D-flow profile obtained from MRI examination.

Lastly, laminar flow was assumed for all simulations. This assumption is commonly used in computational studies and reduces computational costs. From the calculated Reynolds numbers in this study, it is expected that some turbulence is present. However, our use of
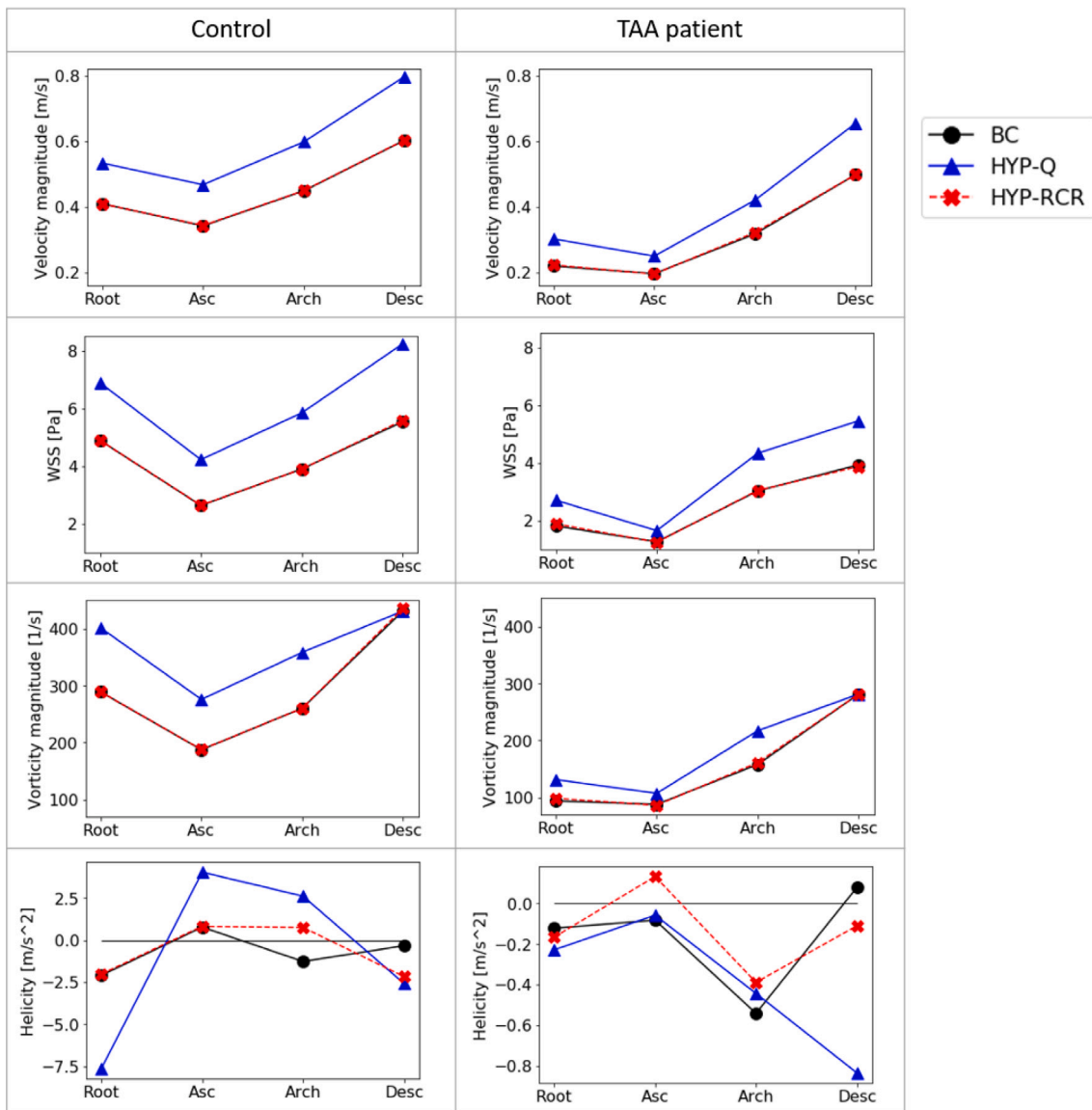
**Fig. 12.** Mean velocity magnitude, WSS magnitude, vorticity magnitude and helicity through the aorta (root, ascending aorta, arch and descending aorta) in control and TAA patient at peak-systole. The graphs depict the base case (BC) and two hypertension models (HYP-Q and HYP-RCR).

sufficiently small time steps and sufficiently fine spatial resolution of the employed mesh (with a local refinement in the wall proximity), enable capturing of the local flow instabilities. Future studies by assessing the Reynolds-Averaged Navier–Stokes (RANS) type of the turbulence models or high-fidelity Large-Eddy Simulations (LES) can be performed under identical flow conditions, but this was outside the scope of the present manuscript.

**5. Conclusions**

The 3EWK model could be used to alter the RCR-parameters individually which resulted in pressure changes during a cardiac cycle. Virtual hypertension was successfully modeled by either increasing inflow with 30% (HYP-Q) or increasing resistance via $1.5 \times R1$, $1.75 \times R2$ and $0.9 \times C$ (HYP-RCR). It was found that pressure could not be increased by increasing only flow rate.

The TAA patient and control were successfully simulated at hypertensive states and responded similarly to virtual hypertension. No major changes in hemodynamic variables were observed in the TAA patient and control when resistance was increased. Regions with high ECAP values reduced in the TAA patient as a result of higher flow rates. If

hypertension occurs due to an increase in flow rate, it is believed that this would not necessarily be an adverse effect for the TAA patient in the context of thrombogenesis risk.

By comparing one TAA patient and one control at normotensive state at peak-systole, helicity and vorticity were found to be lower in the TAA patient throughout the entire domain. The lowest values of vorticity and helicity in the TAA patient were found in the aneurysmatic region. Additionally, regions with high ECAP (close of 1.4 Pa$^{-1}$) were found in a TAA patient in the aneurysmatic region at the outer curvature which could indicate an elevated risk of thrombogenesis. The ECAP values observed in the control were significantly lower (below 0.6 Pa$^{-1}$).

Sole diameter is insufficient in predicting aneurysm growth and complications. Aortic blood flow, however, has been recognized as a potential predictor, [6]. From the current study, it can be concluded that local biomarkers could contribute to better-predicting aneurysm complications. We propose that such biomarkers can be divided into two classes: wall or flow-related. We recommend using ECAP as a wall-related biomarker since it captures both the effect of high OSI and low WSS. Additionally, the Q-criterion could be used to quantify flow structures and assess vortex strength.

**List of abbreviations:**

| | |
|---|---|
| 3EWK | Three-Element Windkessel |
| ABAO | Abdominal Aorta |
| ASC | Ascending Aorta |
| BCT | Brachiocephalic Trunk |
| CFD | Computational Fluid Dynamics |
| DESC | Descending Aorta |
| ECAP | Endothelial Cell Activation Potential |
| GCI | Grid Convergence Index |
| LCCA | Left Common Carotid Artery |
| LSA | Left Subclavian Artery |
| MRI | Magnetic Resonance Imaging |
| OSI | Oscillatory Shear Index |
| PS | Peak Systole |
| TAA | Thoracic Aortic Aneurysm |
| TAWSS | Time-Averaged Wall Shear Stress |
| UDF | User-Defined Function |
| VMTK | Vascular Modeling Toolkit |
| WSS | Wall Shear Stress |

**CRediT authorship contribution statement**

**M.J.F.G. Ramaekers:** Writing – review & editing, Writing – original draft, Investigation, Formal analysis, Data curation, Conceptualization. **I.B. van der Vlugt:** Writing – review & editing, Writing – original draft, Visualization, Validation, Methodology, Investigation, Data curation. **J.J.M. Westenberg:** Writing – original draft, Investigation, Funding acquisition, Data curation. **R. Perinajová:** Writing – original draft, Visualization, Validation, Software, Data curation, Conceptualization. **H.J. Lamb:** Writing – original draft, Supervision, Funding acquisition, Formal analysis. **J.E. Wildberger:** Writing – original draft, Funding acquisition, Formal analysis, Conceptualization. **S. Kenjereš:** Writing – review & editing, Visualization, Validation, Supervision, Software, Resources, Methodology, Investigation, Funding acquisition, Formal analysis, Conceptualization. **S. Schalla:** Writing – review & editing, Writing – original draft, Validation, Supervision, Methodology, Investigation, Formal analysis, Conceptualization.

**Declaration of competing interest**

The authors declare that they have no known competing financial interests or personal relationships that could have appeared to influence the work reported in this paper.

**Acknowledgments**

**Appendix A. Mesh dependency**

In order to assess the accuracy of the simulations, a grid sensitivity analysis was performed. Three different polyhedral meshes were obtained for the computational domain of C3: coarse ($\approx$ 469 K polyhedral elements), medium ($\approx$ 728 K polyhedral elements) and fine ($\approx$ 1.3 mil polyhedral elements). After performing simulations, WSS was compared at peak-systole (during the fifth cycle) as depicted in Fig. A.13 with detail on the ascending aorta. Furthermore, the WSS was extracted over a line (Fig. A.14(a)). The local WSS variation alongside the line is shown in Fig. A.14(b). The horizontal line in the graphs is the average WSS value measured at the polyline. Additionally, the Grid Convergence Index (GCI) is calculated using the average WSS along the line and at the aortic wall to quantify our findings (Table A.6). It is confirmed that the medium mesh is fine enough the generate mesh-independent flow features.
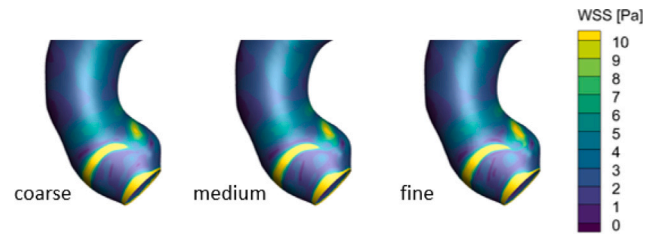


**Fig. A.13.** Wall shear stress (WSS) at peak-systole for the control (C3), using a coarse, medium and fine mesh.
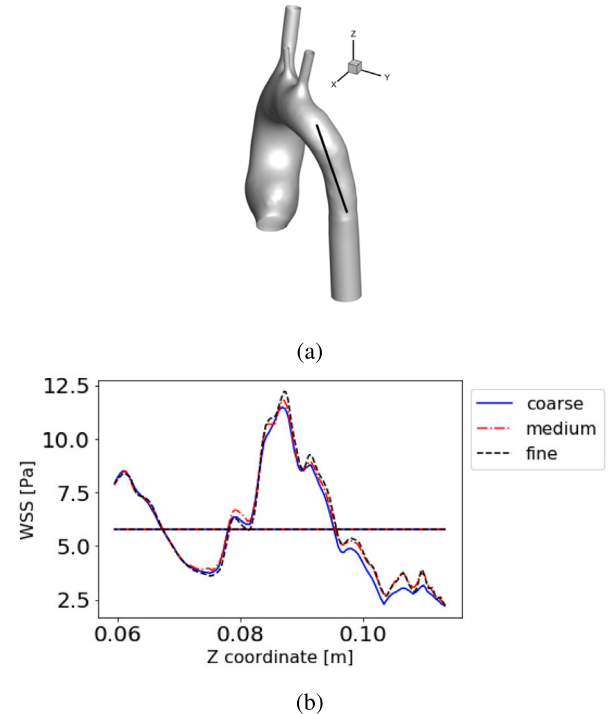


(a)



(b)

**Fig. A.14.** (a) Location of polyline for the control (C3). (b) Variation of WSS along polyline at peak-systole. The horizontal line in (b) is the average WSS value measured at the polyline.

**Table A.6**

Grid Convergence Index (GCI) estimation for the control (C3) at peak-systole. $f_1$ is WSS for the coarse mesh, $f_2$ for the medium mesh and $f_3$ for the fine mesh. r is the refinement ratio and is calculated by $(r_{12} + r_{23})/2$ where $r_{12}$ is the refinement ratio between the coarse and medium mesh and $r_{23}$ between the medium and fine mesh. p is the order of convergence, $f_{h=0}$ is the Richardson solution, $GCI_{1,2}$ is the GCI for the fine and medium mesh, and $GCI_{2,3}$ is the GCI for the medium and coarse mesh.

| | | Line | Wall |
|---|---|---|---|
| $WSS_1$ | [Pa] | 5.56 | 4.42 |
| $WSS_2$ | [Pa] | 5.77 | 4.43 |
| $WSS_3$ | [Pa] | 5.78 | 4.46 |
| r | | 1.18 | 1.18 |
| p | | −21.9 | 7.12 |
| $f_{h=0}$ | [Pa] | 5.77 | 4.47 |
| $GCI_{1,2}$ | [%] | $-4.67 \times 10^{-2}$ | $9.62 \times 10^{-4}$ |
| $GCI_{2,3}$ | [%] | $-1.21 \times 10^{-3}$ | $3.16 \times 10^{-3}$ |
| Asymptotic? | | 1.001 | 0.994 |

**Appendix B. Parametric study of the 3EWK model**

In the present study, we model virtual hypertension by increasing the blood flow resistance by altering the RCR parameters in the 3EWK boundary conditions (indicated as HYP-RCR method). To determine the model response to changes in the RCR parameters, a detailed
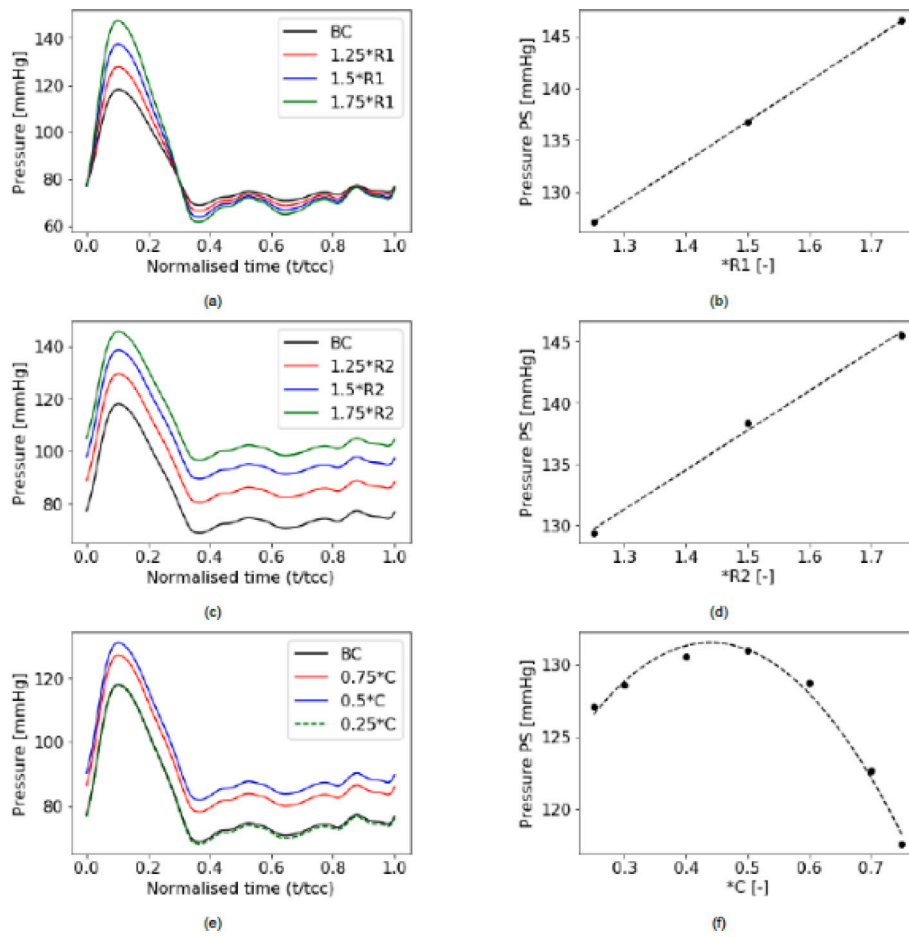
**Fig. B.15.** (a) Change in pressure waveform by increasing proximal resistance (R1). (b) Change in value peak-systole by increasing proximal resistance (R1), ($y = 38.691x + 117.47$, $R^2 = 1$). (c) Change in pressure waveform by increasing peripheral resistance (R2), (d) Change on value peak-systole by increasing peripheral resistance (R2), ($y = 32.317x + 121.61$, $R^2 = 0.9954$). (e) Change in pressure waveform by decreasing compliance (C). (f) Change in value peak-systole by decreasing compliance (C), ($y = 138.12x^2 + 121.44x + 104.85$, $R^2 = 0.9845$). Note that BC indicates the base case, i.e. with not altered values of RCR parameters.
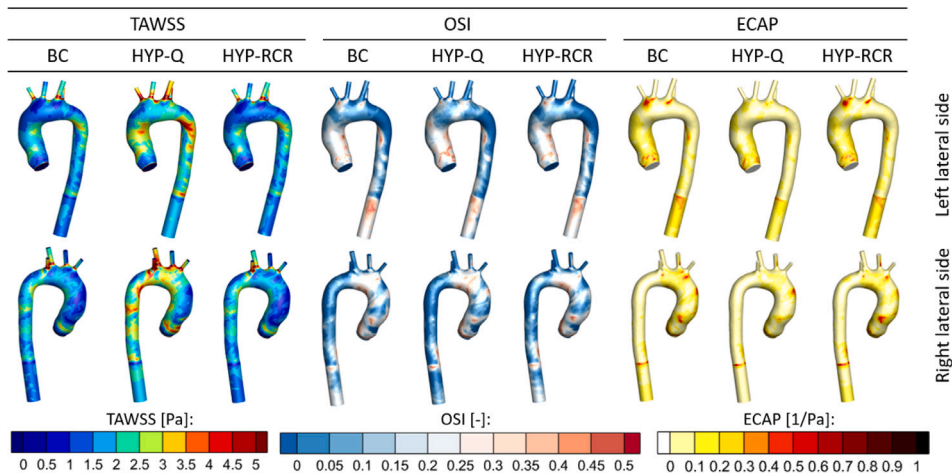


**Fig. C.16.** Time averaged wall shear stress (TAWSS), oscillatory shear index (OSI) and endothelial cells activation potential (ECAP) for the base case (BC) and two hypertension models (HYP-Q and HYP-RCR) in C1.

parametric study is performed for the control group case (C3). Both R1 and R2 resistances were increased by 25%, 50%, and 75%, respectively. Furthermore, compliance (C) was decreased by 25%, 50%, and 75%, respectively. It can be seen that increasing R1 mainly affects the systolic blood pressure, Figs. B.15(a–b). In contrast, increasing R2 resulted

in an upward shift of the entire pressure waveform, Figs. B.15(c–d). A non-linear behavior is observed for altering compliance (C), with a characteristic inflection point around 0.45, Figs. B.15(e–f). It can be concluded that the RCR parameters can be altered individually to mimic the pressure changes during the cardiac cycle.
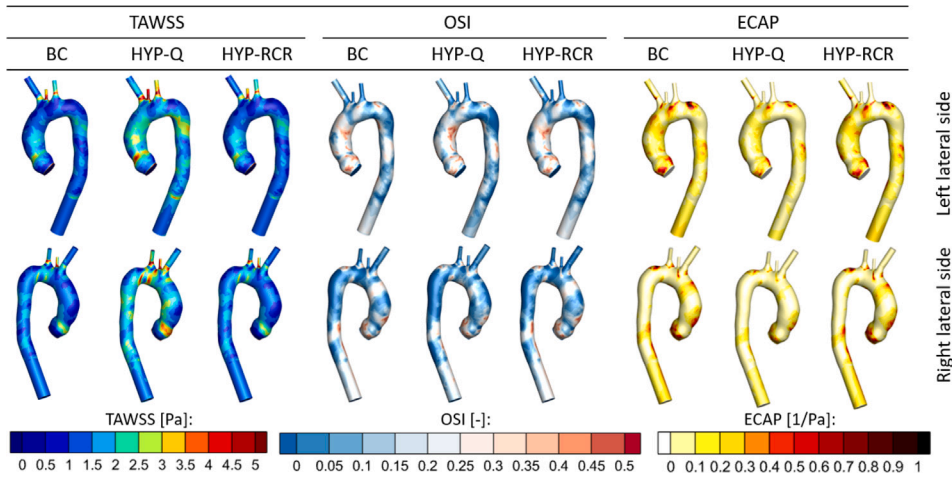
**Fig. C.17.** Time averaged wall shear stress (TAWSS), oscillatory shear index (OSI) and endothelial cells activation potential (ECAP) for the base case (BC) and two hypertension models (HYP-Q and HYP-RCR) in C2.



**Fig. C.18.** Time averaged wall shear stress (TAWSS), oscillatory shear index (OSI) and endothelial cells activation potential (ECAP) for the base case (BC) and two hypertension models (HYP-Q and HYP-RCR) in C4.
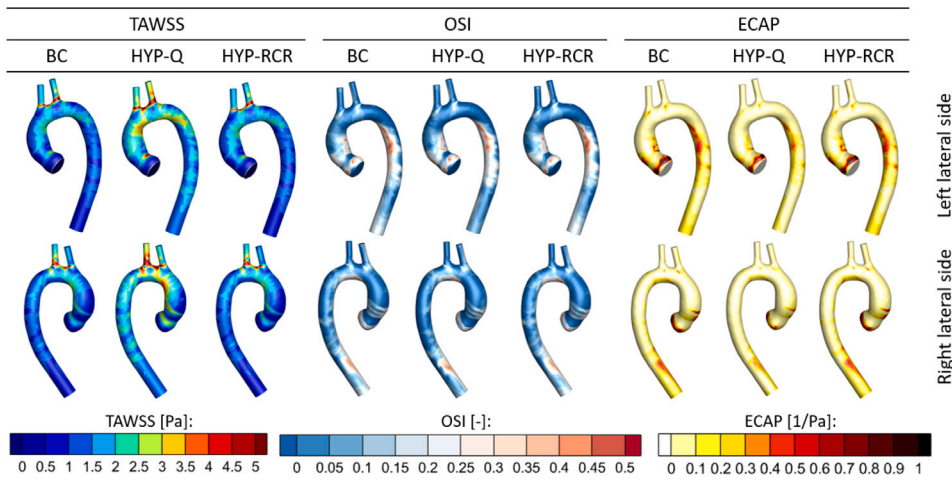


**Fig. C.19.** Time averaged wall shear stress (TAWSS), oscillatory shear index (OSI) and endothelial cells activation potential (ECAP) for the base case (BC) and two hypertension models (HYP-Q and HYP-RCR) in P1.

**Fig. C.20.** Time averaged wall shear stress (TAWSS), oscillatory shear index (OSI) and endothelial cells activation potential (ECAP) for the base case (BC) and two hypertension models (HYP-Q and HYP-RCR) in P2.
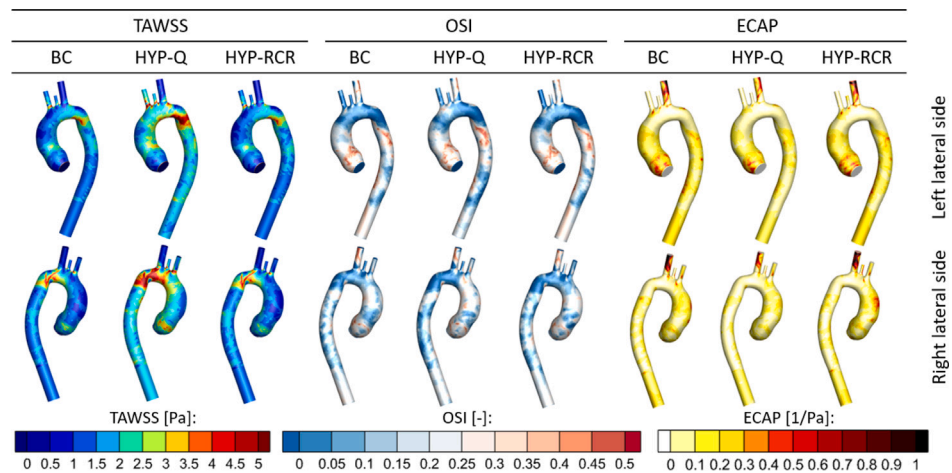


**Fig. C.21.** Time averaged wall shear stress (TAWSS), oscillatory shear index (OSI) and endothelial cells activation potential (ECAP) for the base case (BC) and two hypertension models (HYP-Q and HYP-RCR) in P3.
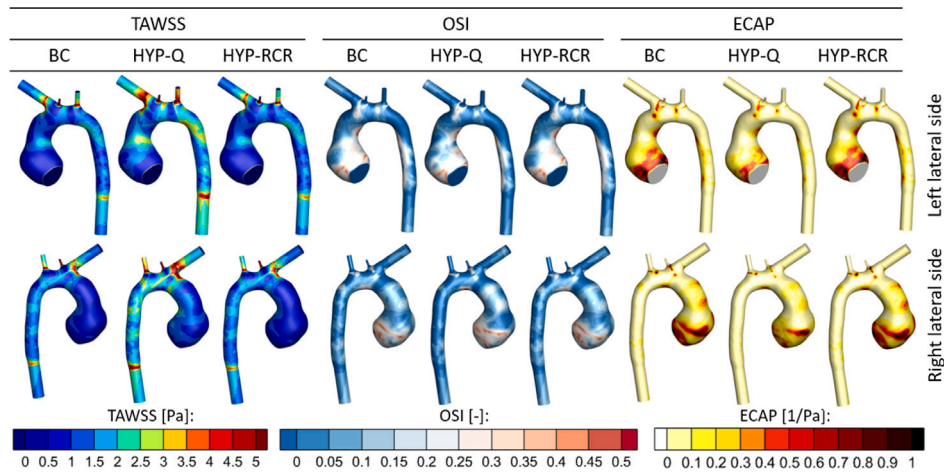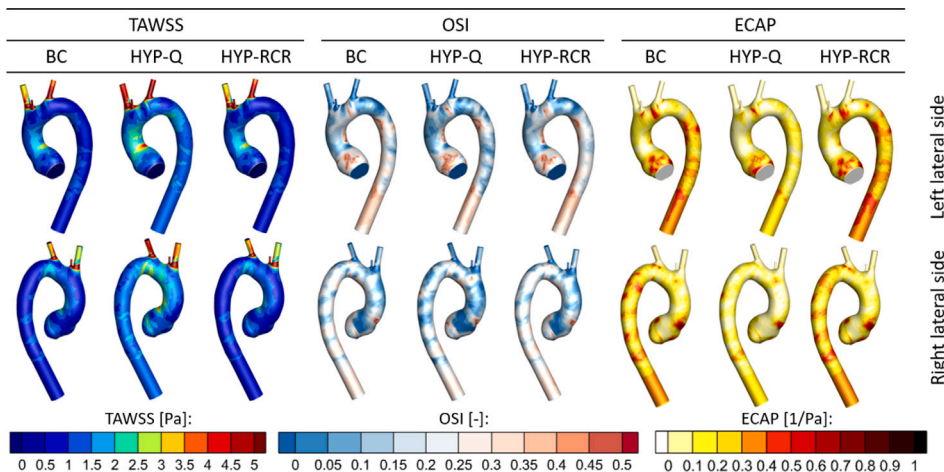
## Appendix C. Remaining cases

One TAA patient and one control have been extensively discussed in the results section. Three additional TAA patients and controls have been simulated to validate whether the present model of hypertension was also applicable to other cases. In total four TAA patients and four controls were included for simulations from which one TAA patient and one control have been extensively discussed in the results section. Hypertensive states were successfully simulated for these cases demonstrating numerical robustness of the present approach. The TAWSS, OSI and ECAP results for the six other cases (C1, C2, C4, P1, P2 and P3) are displayed in Figs. C.16, C.17, C.18, C.19, C.20 and C.21, respectively. These results confirm what we have observed in the TAA patient and control that have been analyzed in this study.

## References

[1] R. Erbel, V. Aboyans, C. Boileau, E. Bossone, R.D. Bartolomeo, H. Eggebrecht, et al., 2014 ESC Guidelines on the diagnosis and treatment of aortic diseases: Document covering acute and chronic aortic diseases of the thoracic and abdominal aorta of the adult. The Task Force for the Diagnosis and Treatment of Aortic Diseases of the European Society of Cardiology (ESC), Eur. Heart J. 35 (41) (2014) 2873–2926.

[2] L.F. Hiratzka, G.L. Bakris, J.A. Beckman, R.M. Bersin, V.F. Carr, D.E. Casey, Jr., et al., ACCF/AHA/AATS/ACR/ASA/SCA/SCAI/SIR/STS/SVM guidelines for the diagnosis and management of patients with thoracic aortic disease, J. Am. Coll. Cardiol. 55 (14) (2010) 27–129.

[3] L.A. Pape, T.T. Tsai, E.M. Isselbacher, J.K. Oh, P.T. O'Gara, A. Evangelista, et al., Aortic diameter ≥ 5.5 cm is not a good predictor of type a aortic dissection: Observations from the International Registry of Acute Aortic Dissection (IRAD), Circulation 116 (10) (2007) 1120–1127.

[4] M.A. Coady, J.A. Rizzo, G.L. Hammond, G.S. Kopf, J.A. Elefteriades, Surgical intervention criteria for thoracic aortic aneurysms: A study of growth rates and complications, Ann. Thoracic Surg. 67 (6) 1922–1926, ; discussion 1953–58 (1999).

[5] J. Bürk, P. Blanke, Z. Stankovic, A. Barker, M. Russe, J. Geiger, et al., Evaluation of 3D blood flow patterns and wall shear stress in the normal and dilated thoracic aorta using flow-sensitive 4D CMR, J. Cardiovasc. Magn. Reson. 14 (84) (2012) 1–11.

[6] B.P. Adriaans, J.E. Wildberger, J.J.M. Westenberg, H.J. Lamb, S. Schala, Predictive imaging for thoracic aortic dissection and rupture: Moving beyond diameters, Eur. Radiol. 29 (12) (2019) 6396–6404.

[7] A. Guala, Dux-Santoy, G. Teixido-Tura, A. Ruiz-Muñoz, L. Galian-Gay, M.L. Servato, et al., Wall shear stress predicts aortic dilation in patients with bicuspid aortic valve, JACC: Cardiovasc. Imaging 15 (1) (2022) 46–57.

[8] S. Ebel, A. Kühn, A. Aggarwal, B. Köhler, B. Behrendt, R. Gohmann, et al., Quantitative normal values of helical flow, flow jets and wall shear stress of healthy volunteers in the ascending aorta, Eur. Radiol. 32 (2022) 8597–8607.

[9] M.J.F.G. Ramaekers, B.P. Adriaans, J.F. Juffermans, H.C. van Assen, S.C.A.M. Bekkers, A.J.H.A. Scholte, et al., Characterization of ascending aortic flow in patients with degenerative aneurysms: A 4D flow magnetic resonance study, Investig. Radiol. 56 (8) (2021) 494–500.

[10] S. Kenjereš, On recent progress in modelling and simulations of multi-scale transfer of mass, momentum and particles in bio-medical applications, Flow Turbul. Combust. 96 (2016) 837–860.

[11] R. Perinajová, J.F. Juffermans, J.J.M. Westenberg, R.L.F. van der Palen, P.J. van den Boogaard, H.J. Lamb, et al., Geometrically induced wall shear stress

variability in CFD-MRI coupled simulations of blood flow in the thoracic aortas, Comput. Biol. Med. 133 (2021) 104385.

[12] R. Perinajová, C.B. Álvarez-Cuevas, J. Juffermans, J. Westenberg, H. Lamb, S. Kenjereš, Influence of aortic aneurysm on the local distribution of NO and O2 using image-based computational fluid dynamics, Comput. Biol. Med. 160 (2023) 106925.

[13] A. Sarami-Foroushani, M.C. Villa-Uriol, M.N. Esfahany, S.C. Coley, L.Y. Di Marco, A.F. Frangi, A. Marzo, Modeling of the acute effects of primary hypertension and hypotension on the hemodynamics of intracranial aneurysms, Ann. Biomed. Eng. 43 (1) (2015) 207–221.

[14] P. Vasava, P. Jalali, M. Dabagh, P.J. Kolari, Finite element modelling of pulsatile blood flow in idealized model of human aortic arch: Study of hypotension and hypertension, Comput. Math. Methods Med. 2012 (2011) 861837.

[15] P.K. Singh, A. Marzo, B. Howard, D.A. Rufenacht, P. Bijlenga, A.F. Frangi, P.V. Lawford, S.C. Coley, D.R. Hose, U.J. Patel, Effects of smoking and hypertension on wall shear stress and oscillatory shear index at the site of intracranial aneurysm formation, Clin. Neurol. Neurosurg. 112 (2010) 306–313.

[16] A. Fuchs, N. Berg, L.P. Wittberg, Pulsatile aortic blood flow - A critical assessment of boundary conditions, J. Eng. Sci. Med. Diagn. Therapy 4 (1) (2021).

[17] J. Lantz, M. Karlsson, Large eddy simulation of LDL surface concentration in a subject specific human aorta, J. Biomech. 45 (3) (2012) 537–542.

[18] I.E. Vignon-Clementel, C.A. Figueroa, K.E. Jansen, C.A. Taylor, Outflow boundary conditions for 3D simulations of non-periodic blood flow and pressure fields in deformable arteries, Comput. Methods Biomech. Biomed. Eng. 13 (5) (2010) 625–640.

[19] L. Antiga, M. Piccinelli, L. Botti, B. Ene-Iordache, A. Remuzzi, D.A. Steinman, An image-based modeling framework for patient-specific computational hemodynamics, Med. Biol. Eng. Comput. 46 (2008) 1097–1112.

[20] S. Chien, Shear dependence of effective cell volume as a determinant of blood viscosity, Science 168 (3934) (1970) 977–979.

[21] A. Deyranlou, Development of a Numerical Workflow to Study Effects of Atrial Fibrillation on Cardiovascular Circulation (Doctoral dissertation), University of Manchester, U.K., 2021.

[22] J. Mayet, A. Hughes, Cardiac and vascular pathophysiology in hypertension, Heart 89 (9) (2004) 1104–1109.

[23] S. Sethi, O. Rivera, R. Oliveros, R. Chilton, Aortic stiffness: Pathophysiology, clinical implications, and approach to treatment, Integr. Blood Pressure Control 7 (2014) 29–34.

[24] E.S. Kröner, H.J. Lamb, H.M. Siebelink, S.C. Cannegieter, P.J. van den Boogaard, E.E. van der Wall, et al., Pulse wave velocity and flow in the carotid artery versus the aortic arch: Effects of aging, J. Magn. Reson. Imaging 40 (2) (2014) 287–293.

[25] B. Doyle, K. Miller, A. Wittek, P.M.F. Nielsen, Computational Biomechanics for Medicine, Springer, New York, 2014.

[26] G.S. Worthen, L.A. Smedly, M.G. Tonnesen, D. Ellis, N.F. Voelkel, J.T. Reeves, P.M. Henson, Effects of shear stress on adhesive interaction between neutrophils and cultured endothelial cells, J. Appl. Physiol. 63 (5) (1987) 2031–2041.

[27] H. Meng, V.M. Tutino, J. Xiang, A. Siddiqui, High WSS or low WSS? Complex interactions of hemodynamics with intracranial aneurysm initiation, growth, and rupture: Toward a unifying hypothesis, Am. J. Neuroradiol. 35 (7) (2014) 1254–1262.

[28] D.M. Sforza, C.M. Putman, J.R. Cebral, Hemodynamics of cerebral aneurysms, Annu. Rev. Fluid Mech. 41 (2009) 91–107.

[29] C. Cheng, D. Tempel, R. van Haperen, A. van der Baan, F. Grosveld, M.J. Daemen, et al., Atherosclerotic lesion size and vulnerability are determined by patterns of fluid shear stress, Circulation 113 (23) (2006) 2744–2753.

[30] J.M. Dolan, J. Kolega, H. Meng, High wall shear stress and spatial gradients in vascular pathology: A review, Ann. Biomed. Eng. 41 (7) (2013) 1411–1427.

[31] S. Kenjereš, A. de Loor, Modelling and simulation of low-density lipoprotein transport through multi-layered wall of an anatomically realistic carotid artery bifurcation, J. R. Soc. Interface 11 (2014) 20130941.

[32] S. Kenjereš, J.P. van der Krieke, C. Li, Endothelium resolving simulations of wall shear-stress dependent mass transfer of LDL in diseased coronary arteries, Comput. Biol. Med. 114 (2019) 103453.

[33] A.J. Boyd, D.C. Kuhn, R.J. Lozowy, G.P. Kulbisky, Low wall shear stress predominates at sites of abdominal aortic aneurysm rupture, J. Vasc. Surg. 63 (6) (2016) 1613–1619.

[34] J. von Spiczak, G. Crelier, D. Giese, S. Kozerke, D. Maintz, A.C. Bunck, Quantitative analysis of vortical blood flow in the thoracic aorta using 4D phase contrast MRI, PLoS One 10 (9) (2015) e0139025.

[35] F.M. Callaghan, P. Bannon, E. Barin, D. Celemajer, R. Jeremy, G. Figtree, S.M. Grieve, Age-related changes of shape and flow dynamics in healthy adult aortas: A 4D flow MRI study, J. Magn. Reson. Imaging 49 (1) (2019) 90–100.

[36] D.N. Ku, Blood flow in arteries, Annu. Rev. Fluid Mech. 29 (1) (1997) 399–434.

[37] K.M. Khanafer, P. Gadhoke, R. Berguer, J.L. Bull, Modeling pulsatile flow in aortic aneurysms: Effect of non-Newtonian properties of blood, Biorheology 43 (5) (2006) 661–679.

[38] S.Z. Zhao, X.Y. Xu, A.D. Hughes, S.A. Thom, A.V. Stanton, B. Ariff, Q. Long, Blood flow and vessel mechanics in a physiologically realistic model of a human carotid arterial bifurcation, J. Biomech. 33 (8) (2000) 975–984.

[39] D. Zeng, E. Boutsianis, M. Ammann, K. Boomsma, S. Wildermuth, D. Poulikakos, A study on the compliance of a right coronary artery and its impact on wall shear stress, J. Biomech. Eng. 130 (4) (2008) 041014.

[40] D.N. Ku, D.P. Giddens, C.K. Zarins, S. Glagov, Pulsatile flow and atherosclerosis in the human carotid bifurcation, positive correlation between plaque location and low oscillating shear stress, Arterioscler Thromb. Vasc. Biol. 5 (3) (1985) 293–302.

[41] M. Dabagh, P. Jalali, Y.T. Konttinen, P. Sarkomaa, Distribution of shear stress over smooth muscle cells in deformable arterial wall, Med. Biol. Eng. Comput. 46 (7) (2008) 649–657.

[42] B.A. Towfiq, J. Weir, J.M. Rawles, Effect of age and blood pressure on aortic size and stroke distance, Brit. Heart J. 55 (6) (1986) 560–568.

[43] P. Youssefi, A. Gomez, C. Arthurs, R. Sharma, M. Jahangiri, C. Alberto Figueroa, Impact of patient-specific inflow velocity profile on hemodynamics of the thoracic aorta, J. Biomech. Eng. 140 (1) (2017) 011002.

[44] S. Madhavan, E.M.C. Kemmerling, The effect of inlet and outlet boundary conditions in image-based CFD modeling of aortic flow, BioMed. Eng. OnLine 17 (66) (2018).

[45] U. Morbiducci, R. Ponzini, D. Gallo, C. Bignardi, G. Rizzo, Inflow boundary conditions for image-based computational hemodynamics: Impact of idealized versus measured velocity profiles in the human aorta, J. Biomech. 46 (1) (2013) 102–109.